Journal of Computational Physics **173,** 322–347 (2001)
doi:10.1006/jcph.2001.6879, available online at http://www.idealibrary.com on IDEAL®

Simulation of Pollutant Transport Using a Particle Method

S. Zimmermann,* P. Koumoutsakos,† and W. Kinzelbach*

**Institute of Hydromechanics and Water Resources Management (IHW), ETH Hönggerberg, Zürich CH-8093, Switzerland; and †Institute of Computational Sciences, ETH, Zürich CH-8092, Switzerland, and CTR, NASA Ames 202A-1, Moffett Field, California 94035*

E-mail: zimmermann@ihw.baug.ethz.ch, petros@inf.ethz.ch, kinzelbach@ihw.baug.ethz.ch

Received December 11, 2000; revised July 5, 2001

A Lagrangian scheme is presented for the two-dimensional simulation of pollutant transport in a porous medium. The anisotropic extension of the particle strength exchange method is implemented to describe the diffusive–dispersive process. By applying the scheme to a benchmark problem with an analytical solution, the method is shown to be accurate and stable even in the limiting cases of vanishing diffusion–dispersion coefficients and high anisotropy ratios. The scheme is shown to perform well with spatially variable velocity fields also.

Key Words: diffusion; particle methods.

1. INTRODUCTION

This article is concerned with the numerical simulation of pollutant transport in groundwater using a Lagrangian scheme, based on a particle method. The grid-free character of the particle methods and the straightforward physical interpretation of their results make them an interesting alternative to established methods such as finite differences or finite elements. Drawbacks such as computational cost and difficulties in dealing with diffusive effects have been overcome by the development of fast summation algorithms [9] and recent developments in new numerical methods for the accurate treatment of diffusive effects. In the past, diffusion was generally added to Lagrangian particle methods using the random walk method introduced by Chorin [2] in 1973. This method is stable and easy to implement but has the disadvantage of a relatively low convergence rate. In the 80's, an alternative scheme, the particle strength exchange method (PSE), was introduced by Mas-Gallic [17] and coworkers (Cottet [3], Huberson [10], Raviart [19]). This method accounts for diffusive effects by approximating the differential diffusion operator by an integral operator which when discretized, using as quadrature points the locations of the particles, amounts to a redistribution of the particle strengths. Practical implementations of the theory of particle

0021-9991/01 $35.00

strength exchange (for examples see Winckelmans [22], Winckelmans and Leonard [23], Koumoutsakos and Leonard [15]) deal with a scalar isotropic diffusion parameter as described in Degond and Mas-Gallic [7]. In a second step, Degond and Mas-Gallic extended their theory to the case of an anisotropic (matrix) diffusion parameter [8]. However, we are not aware of any practical implementations or numerical studies using this anisotropic extension of the PSE theory.

The macroscopic transport of a nonreactive solute in a porous medium can be described by three main transport processes: the advective motion with the mean velocity field of the flow, the molecular diffusion, and the dispersion of the pollutant. Molecular diffusion is only important at a microscopic scale and is generally incorporated in the dispersive mass flux. Both diffusion and dispersion may be described in a first approximation by Fick's law. The dispersive flux is due to subscale variations in velocity caused by the varying thickness of pores, the bending of streamlines around the grains, the variation of the velocity profiles within the pores, and the inhomogeneities of the aquifer. Dispersion is always anisotropic even in the case of an isotropic medium and at least one order of magnitude larger in flow direction than orthogonal to the flow direction. Dispersion has to be described by a tensor of second rank. Depending on the proportions of the advective and the dispersive flux—characterized by the Peclet number $Pe = \frac{Lu}{D_L}$, with L some characteristic length of the transport phenomenon, u the mean velocity, and D_L the dispersion coefficient—the transport equation shows a more hyperbolic (high Peclet number) or a more parabolic (low Peclet number) character.

First implementations of a numerical solution to the advection–dispersion transport equation were realized with finite difference (FD) and finite element (FE) methods. For a review of analytical and numerical transport modelling in groundwater see Kinzelbach [13]. The discretization restrictions and difficulties associated with the hyperbolic aspect of the transport equation, as well as the problems of numerical dispersion and numerical oscillations associated with FD and FE schemes, gave rise to the development of the method of characteristics (MOC) [1] and random walk schemes [12, 21].

These particle-based methods avoid many of the problems arising in FD and FE methods. The grid anisotropy problems that FD and FE methods experience in the case when the mean flow direction is not aligned with a grid direction do not show up with particle-based methods. The limiting case of disappearing dispersivities (high Peclet number flows) and the case of scale-dependent dispersivities can only be treated well by random walk methods. However, there are shortcomings with the method of characteristics and the random walk as well. The method of characteristics has problems in dealing with high anisotropy ratios (when the longitudinal dispersivity is two or more orders of magnitude larger than the transversal dispersivity). In its implementation using particles, it also suffers from synchronization effects of the tracer particle movement which may lead to nonphysical oscillations. The random walk method, on the other hand, gives a very rough picture of the concentration distribution due to the stochastic nature of the dispersive step.

The PSE method with the anisotropic extension of Degond and Mas-Gallic [8] shares the advantages of the random walk method without having the disadvantage of the stochastical oscillations, as the integral operator replacing the differential diffusion–dispersion operator results in a higher accuracy for the discretization. In contrast to the method of characteristics, particles are only needed in locations where there is solute. Since the PSE method avoids artificial mixing of the concentrations while preserving the local gradients, sharp fronts and high anisotropy ratios can be well simulated. This is especially important in groundwater

applications where concentration fronts stay relatively sharp and in natural heterogeneous media where a smooth concentration distribution is only reached in the long time limit.

In the present work the numerical scheme originally developed for viscous fluid flow carrying vorticity [14] is used as a basis for the 2D simulation of passive pollutant transport in groundwater. We presume an externally given (mean) velocity field and treat the advection–dispersion transport equation by means of a particle method with the anisotropic PSE approach describing the diffusive–dispersive process. A validation study, varying the numerical parameters, is conducted to assess the accuracy of the method. The method is applied to a benchmark problem and compared with the analytical solution. As shown in this paper, the PSE scheme is a very accurate and stable method even in the cases of high anisotropy ratios and vanishing dispersivities. In simulations with a more complex flow topology we show that the method is well capable of handling spatially variable diffusion–dispersion tensors.

The paper is organized as follows: In Section 2 the governing equations and the numerical method are summarized. In Section 3 a validation study is presented. Simulations conducted with a spatially nonconstant velocity field are presented in Section 4. In Section 5 we summarize the present work and discuss its advantages and drawbacks.

2. THE GOVERNING EQUATIONS

2.1. The Advection–Dispersion Equation

Nonreactive solute transport in a porous medium can be described by the advection–dispersion equation,

$$\frac{\partial c(\mathbf{x}, t)}{\partial t} + \nabla(\mathbf{u}(\mathbf{x}, t) \cdot c(\mathbf{x}, t)) - \sigma(\mathbf{x}, t) = \nabla(\mathbf{D}(\mathbf{x}, t) \cdot \nabla c(\mathbf{x}, t)), \tag{1}$$

where $\mathbf{u}$ is a given mean velocity field, c stands for the tracer concentration, σ is a term for internal sources and sinks, and $\mathbf{D}$, a symmetric tensor of second rank, contains diffusion and dispersion.

The numerical method presented here is based on the discretization of the above equation in a Lagrangian frame using a particle method. The advection–dispersion equation (Eq. (1)) may thus be transformed into the set of equations

$$\frac{d\mathbf{x}}{dt} = \mathbf{u}(\mathbf{x}, t) \tag{2}$$

$$\frac{dc(\mathbf{x}, t)}{dt} = \nabla(\mathbf{D}(\mathbf{x}, t) \cdot \nabla c(\mathbf{x}, t)) + \sigma(\mathbf{x}, t), \tag{3}$$

with $\mathbf{u}(\mathbf{x}, t)$ a given external mean velocity field which moves the particles along their characteristics.

2.2. Particle Strength Exchange (PSE)

The particle strength exchange method (PSE) was introduced by Mas-Gallic [17] and coworkers (Cottet [3], Huberson [10], Raviart [19]). This method accounts for diffusive effects by appropriately modifying the strength of the particles. It is based on the approximation of the diffusion operator of the advection–diffusion transport equation by an integral

operator and the application of a quadrature rule to this integral using as quadrature points the locations of the particles. Each particle is characterized by a regularization function. In order to maintain stability and accuracy, the particles' regularization functions must overlap at all times [14]. Therefore the particle field must be occasionally remeshed onto a new structured field depending on the map of the flow field. As Koumoutsakos [14] showed, the accuracy of the PSE method is more than two orders of magnitude superior to the random walk method. For a special kernel and in case the particles occupy regular positions on the grid, Cottet [4] showed that the method is equivalent to a second order finite-difference approximation. For the reader's convenience we summarize the important steps of the PSE method for both the isotropic and the anisotropic case. For further details see [7] and [8].

2.2.1. *The Isotropic Case*

In the first part of their paper [7], Degond and Mas-Gallic proposed a new particle approximation for the isotropic diffusion part of the general advection–diffusion equation. Note that the diffusion part of the advection–diffusion equation corresponds to the dispersion part of the advection–dispersion equation (Eq. (1)). In the isotropic case the diffusion matrix **D** can be replaced by a scalar function $\nu(x)$. If the kernel σ^ε satisfies certain moment conditions, Taylor's formula shows [7] that the integral operator is an approximation of the differential diffusion operator:

$$\nabla(\nu\nabla c) \approx \nu Q^\varepsilon(t)c(\mathbf{x},t) = \nu\int_{\Re^2}\sigma^\varepsilon(\mathbf{x},\mathbf{y},t)[c(\mathbf{y})-c(\mathbf{x})]\,d\mathbf{y}. \tag{4}$$

In particle methods the concentration field may be expressed as a discrete sum of the concentrations of each particle having core radius ε, concentration *c(t)*, and an individual concentration distribution (a regularization function) determined by the function ζ_ε so that

$$c(\mathbf{x},t) = \sum_{i=1}^{N} c_i(t)\zeta_\varepsilon(\mathbf{x}-\mathbf{x}_i(t)), \tag{5}$$

where N is the number of particles employed in the discretization, and $\mathbf{x}_i(t)$ is the position of the i-th particle at time t. The discretized particle approximation Q_h^ε is obtained by applying a quadrature rule to the integral operator $Q^\varepsilon(t)$ using the particles as quadrature points,

$$\bar{Q}_h^\varepsilon(t)c_k(t) = \sum_l \sigma^\varepsilon(\mathbf{x}_k(t),\mathbf{x}_l(t),t)[c_l(t)-c_k(t)]\cdot h^2, \tag{6}$$

where h is the representative interparticle spacing and $\sigma^\varepsilon(\mathbf{x}_k,\mathbf{x}_l)$ is a regularization (smoothing) function which is defined by

$$\sigma^\varepsilon(\mathbf{x}_k,\mathbf{x}_l) = \frac{1}{\varepsilon^2}\eta_\varepsilon(\mathbf{x}_k-\mathbf{x}_l), \quad \eta_\varepsilon(\mathbf{x}) = \frac{1}{\varepsilon^2}\eta\left(\frac{\mathbf{x}}{\varepsilon}\right). \tag{7}$$

If the function $\eta(\mathbf{x})$ obeys the moment conditions

$$\int x_i x_j \eta(\mathbf{x})\,d\mathbf{x} = 2\delta_{ij} \quad \text{for } i,\ j = 1,2$$

$$\int x_1^{i_1}x_2^{i_2}\eta(\mathbf{x})\,d\mathbf{x} = 0 \quad \text{if } i_1+i_2 = 1 \text{ or } 3 \le i_1+i_2 \le r+1, \quad i_1,i_2 \in \mathbf{N}_0, \tag{8}$$

then Taylor's formula shows [7] that the integral operator is an approximation of the diffusion operator to the order r:

$$Q^\varepsilon c = \nabla(\nu \nabla c) + \mathcal{O}(\varepsilon^r), \quad r \geq 2. \tag{9}$$

The discretization of the integral operator Q^ε by the numerical quadrature rule introduces an additional error of $\mathcal{O}(h^k/\varepsilon^{k+1})$ where h is a representative interparticle spacing and k is dependent on the properties of the smoothing function η_ε. The method has been shown to be stable [7] for positive second order regularization functions. The method is also stable for all higher order regularization functions provided there is a positive constant C_o such that

$$\nu \leq C_o \varepsilon^2. \tag{10}$$

The total error induced by the approximation of the diffusion operator and the particle-discretization is of order $\mathcal{O}(\varepsilon^r + \frac{h^k}{\varepsilon^{k+1}})$. Finally, the discretized form of Eq. (3) may be expressed as

$$\frac{dc_k}{dt} = \frac{\nu h^2}{\varepsilon^2} \sum_{l=1}^{N} (c_l - c_k) \eta_\varepsilon(\mathbf{x}_k - \mathbf{x}_l) + \sigma(\mathbf{x}, t). \tag{11}$$

2.2.2. *The Anisotropic Case*

In [8], Degond and Mas-Gallic extended their earlier approximation of the diffusion operator by an integral operator from the isotropic to the anisotropic case. Together with more severe restrictions on the regularization function within the integral operator they find the need to use different regularization functions for each component of the dispersion tensor due to the appearance of the mixed derivative terms.

In general form, the dispersion tensor in 2D may be written as

$$\mathbf{D} = \begin{pmatrix} D_{xx} & D_{xy} \\ D_{yx} & D_{yy} \end{pmatrix}, \tag{12}$$

where, according to Scheidegger [18],

$$\begin{aligned} D_{xx} &= \alpha_L \frac{\mathbf{u}_x^2}{|\mathbf{u}|} + \alpha_T \frac{\mathbf{u}_y^2}{|\mathbf{u}|} \\ D_{xy} &= D_{yx} = (\alpha_L - \alpha_T) \frac{\mathbf{u}_x \cdot \mathbf{u}_y}{|\mathbf{u}|} \\ D_{yy} &= \alpha_T \frac{\mathbf{u}_x^2}{|\mathbf{u}|} + \alpha_L \frac{\mathbf{u}_y^2}{|\mathbf{u}|} \\ |\mathbf{u}| &= \sqrt{\mathbf{u}_x^2 + \mathbf{u}_y^2}. \end{aligned} \tag{13}$$

α_L and α_T are the longitudinal and transversal dispersivities, respectively. Usually α_L is one order of magnitude larger than α_T. In the most general form, the 2D dispersion equation can be written as

$$\frac{dc(\mathbf{x}, t)}{dt} = \sum_{i,j=1}^{2} \frac{\partial}{\partial \mathbf{x}_i} \left(\mathbf{D}_{ij}(\mathbf{x}, t) \cdot \frac{\partial c(\mathbf{x}, t)}{\partial \mathbf{x}_j} \right). \tag{14}$$

The anisotropic dispersion operator $\nabla(\mathbf{D}\nabla c(\mathbf{x}, t))$ is approximated by an integral operator of the form

$$\nabla(\mathbf{D}\nabla c(\mathbf{x}, t)) \approx Q^{\varepsilon}(t)c(\mathbf{x}, t) = \int_{\Re^2} \sigma^{\varepsilon}(\mathbf{x}, \mathbf{y}, t)[c(\mathbf{y}) - c(\mathbf{x})]\, d\mathbf{y}. \tag{15}$$

The discretized form then reads

$$\bar{Q}_h^{\varepsilon}(t)c_k(t) = \sum_l \sigma^{\varepsilon}(\mathbf{x}_k(t), \mathbf{x}_l(t), t)[c_l(t) - c_k(t)] \cdot h^2, \tag{16}$$

with

$$\sigma^{\varepsilon}(\mathbf{x}_k, \mathbf{x}_l, t) = \frac{1}{\varepsilon^2} \sum_{i,j=1}^{2} M_{ij}(\mathbf{x}_k, \mathbf{x}_l, t)\psi_{ij}^{\varepsilon}(\mathbf{x}_l - \mathbf{x}_k) \tag{17}$$

and

$$\psi_{ij}^{\varepsilon}(\mathbf{x}) = \frac{1}{\varepsilon^2}\psi_{ij}\left(\frac{\mathbf{x}}{\varepsilon}\right),$$

where ψ_{ij}^{ε} is a matrix cut-off (smoothing) function and $M_{ij}(\mathbf{x}, \mathbf{y}, t)$ is a function of the dispersion tensor $\mathbf{D}_{ij}$. In their article Degond and Mas-Gallic [8] propose several methods and examples for practical numerical schemes. Choosing the matrix cut-off function in the form of

$$\psi_{ij}(\mathbf{x}, \mathbf{y}) = \frac{1}{\varepsilon^4}\bar{\Theta}\left(\frac{|\mathbf{x} - \mathbf{y}|}{\varepsilon}\right) \cdot \sum_{i,j=1}^{2} (\mathbf{x} - \mathbf{y})_i (\mathbf{x} - \mathbf{y})_j, \tag{18}$$

we obtain the following discretized form of Eq. (14):

$$\frac{dc_k}{dt} = \frac{h^2}{\varepsilon^6} \sum_{l=1}^{N} (c_l - c_k)\bar{\Theta}\left(\frac{|\mathbf{x}_k - \mathbf{x}_l|}{\varepsilon}\right) \cdot \sum_{i,j=1}^{2} \mathbf{M}_{ij}(\mathbf{x}_k, \mathbf{x}_l)(\mathbf{x}_k - \mathbf{x}_l)_i (\mathbf{x}_k - \mathbf{x}_l)_j. \tag{19}$$

In our numerical simulations we used the following normalized second (Eq. (20)), fourth (Eq. (21)), and 6th (Eq. (22)) order cut-off functions:

$$\bar{\Theta}\left(\frac{|\mathbf{x}_k - \mathbf{x}_l|}{\varepsilon}\right) = \frac{1}{2\pi} e^{-\frac{(\mathbf{x}_k - \mathbf{x}_l)^2}{2\varepsilon^2}} \tag{20}$$

$$\bar{\Theta}\left(\frac{|\mathbf{x}_k - \mathbf{x}_l|}{\varepsilon}\right) = \frac{1}{2\pi} e^{-\frac{(\mathbf{x}_k - \mathbf{x}_l)^2}{2\varepsilon^2}} \left[4 - \frac{(\mathbf{x}_k - \mathbf{x}_l)^2}{2\varepsilon^2}\right] \tag{21}$$

$$\bar{\Theta}\left(\frac{|\mathbf{x}_k - \mathbf{x}_l|}{\varepsilon}\right) = \frac{1}{4\pi} e^{-\frac{(\mathbf{x}_k - \mathbf{x}_l)^2}{2\varepsilon^2}} \left[20 - 10\frac{(\mathbf{x}_k - \mathbf{x}_l)^2}{2\varepsilon^2} + \left(\frac{(\mathbf{x}_k - \mathbf{x}_l)^2}{2\varepsilon^2}\right)^2\right]. \tag{22}$$

Degond and Mas-Gallic [8] suggest $\mathbf{M}(\mathbf{x}_k, \mathbf{x}_l, t)$ to be in the form of

$$\mathbf{M}(\mathbf{x}_k, \mathbf{x}_l) = \frac{1}{2}(\mathbf{m}(\mathbf{x}_k) + \mathbf{m}(\mathbf{x}_l)), \tag{23}$$

where

$$\mathbf{m} = \mathbf{D} - \frac{1}{4} Tr(\mathbf{D}) \cdot \mathbf{I}. \tag{24}$$

Tr stands for the trace of the matrix, and **I** for the identity matrix. With our dispersion matrix

$$\begin{pmatrix} D_{xx} & D_{xy} \\ D_{yx} & D_{yy} \end{pmatrix},$$

we get

$$\mathbf{m}_{ij} = \begin{pmatrix} \frac{1}{4}(3D_{xx} - D_{yy}) & D_{xy} \\ D_{yx} & \frac{1}{4}(3D_{yy} - D_{xx}) \end{pmatrix}. \tag{25}$$

2.3. Lagrangian Distortion–Remeshing

In order to model diffusion–dispersion properly according to the PSE method, the regularization functions of the particles should overlap at all times. Where particles cease to overlap, an exchange of concentration strength is no longer possible. Particle accumulation, on the other hand, leads to numerical instabilities related to the explicit time discretization of the diffusion term [5]. So when the flow field topology leads to clustering or spreading of the particles, a reinitialization of the particle locations onto a new (uniform) grid has to be undertaken. The old concentration field (c) and the distorted particle locations ($\mathbf{x}$) are interpolated to the new grid (particle) locations ($\tilde{\mathbf{x}}$) and the new concentration field ($\tilde{c}$) by means of an appropriate fourth order interpolation kernel $M_4'(u)$, $u = \frac{|\mathbf{x}|}{h}$, where h is the spacing of the new grid, according to

$$\tilde{c}_i(\tilde{\mathbf{x}}_i) \approx \sum_{j=1}^{M} c_j(\mathbf{x}_j) \cdot M_4'\left(\frac{|\tilde{\mathbf{x}}_i - \mathbf{x}_j|}{h}\right), \tag{26}$$

with

$$M_4'(u) = \begin{cases} 1 - \frac{5u^2}{2} + \frac{3u^3}{2} & \text{if } 0 \le u \le 1, \\ \frac{1}{2}(2-u)^2(1-u) & \text{if } 1 \le u \le 2, \\ 0 & \text{if } u > 2. \end{cases} \tag{27}$$

Note that the process is not of the usual interpolation type, as it is complicated by the fact that the old particle locations are disordered. For a more detailed review of interpolation methods see Cottet and Koumoutsakos [6]. The remeshing procedure introduces numerical errors into the scheme. However, when we implement interpolation kernels that conserve the angular impulse, the remeshing does not introduce a second order diffusive error. Moreover, in [16] it is shown that the error introduced by the remeshing is in general smaller than the numerical dissipation error introduced by the time integration (using a second order Adams–Bashforth scheme) of the system of Eqs. (2) and (3). The minimal necessary remeshing frequency is governed by the topology of the flow field considered in the simulation. For most practical simulations remeshing is usually not necessary at each time step. In our simulations we used a remeshing period of one or two time steps (see also Table II). It should be emphasized that for uniform velocity fields there is absolutely no need for remeshing.

3. VALIDATION STUDIES

In this section we examine the implementation of the anisotropic dispersion case described in Section 2.2.2. We consider an unbounded domain with a given constant velocity field. A momentary pollutant source with a Gaussian distribution is injected into the domain. For all simulations a second order Runge–Kutta scheme has been used to advect the particle locations. For this simple case, the transport equation can be solved analytically. The analytical solution for the concentration of an instantaneous Gaussian input may be expressed as

$$c(\boldsymbol{x}, \boldsymbol{y}, t) = \frac{\Delta M}{2\pi m n_e \sqrt{4t^2\left(D_{xx}D_{yy} - D_{xy}^2\right) + \varepsilon_{src}^4 + 2\varepsilon_{src}^2 t(D_{xx} + D_{yy})}} \cdot \exp(A), \quad (28)$$

where

$$A = \left(\frac{-\boldsymbol{x}_t{}^2\left(2tD_{yy} + \varepsilon_{src}^2\right) - \boldsymbol{y}_t{}^2\left(2tD_{xx} + \varepsilon_{src}^2\right) + \boldsymbol{x}_t\boldsymbol{y}_t 4tD_{xy}}{8t^2\left(D_{xx}D_{yy} - D_{xy}^2\right) + 2\varepsilon_{src}^4 + 4\varepsilon_{src}^2 t(D_{xx} + D_{yy})} \right)$$

with

$$\boldsymbol{x}_t = \boldsymbol{x} - \boldsymbol{u}_x t$$
$$\boldsymbol{y}_t = \boldsymbol{y} - \boldsymbol{u}_y t,$$

where ΔM denotes the input of pollutant mass at time t = 0 (momentary injection), m is the thickness of the saturated flow, n_e is the effective porosity, and ε_{src} is the width of the Gaussian input. We compare the numerical solutions c^{nu} with the exact solution c^{ex} by plotting the error either (I),

$$\text{error} = \frac{\sum_{i=1}^{M}\left(c_i^{ex} - c_i^{nu}\right)^2}{M} \quad \text{(I)}$$

summing over the particle locations $x_i (i = 1, \ldots\ldots, M)$, where M is the number of points with $c \geq 10^{-6}$ mg/l, or (II) the relative error at point x_i:

$$\text{rel. error} = \frac{c_{x_i}^{ex} - c_{x_i}^{nu}}{c_{x_i}^{ex}}. \quad \text{(II)}$$

We structure our approach as follows: First we examine the convergence behaviour for varying time step size, core size, and various forms of the dispersion tensor **D** in simulations up to 200 days. Then we show comparisons of the numerical and analytical results with contour plots and breakthrough curves for different anisotropy ratios and remeshing frequencies in simulations up to 1000 days. For comparison purposes one test case (case 8) is also calculated with a finite difference code (MT3DMS). Finally the influence of the order of the cutoff function $\bar{\Theta}$ (Eqs. (20)–(22)) is examined for different anisotropy ratios.

3.1. The Influence of the Core Size and the Time Step Size

Five test cases were chosen with the parameters shown in Table I. The test cases are distinguished by the flow direction—and thus by the form of the dispersion tensor—as well

TABLE I
Parameters Used for the Convergence Study

Case	u_x [m/d]	u_y [m/d]	α_L [m]	α_T [m]	Form of **D** [m^2/d]	Flow direction to the x-axis (degree)	M_{in} [g]
1	1	0	10	1	$\begin{pmatrix} a & 0 \\ 0 & b \end{pmatrix}$	0	125,000
2	$\frac{1}{2}\sqrt{2}$	$-\frac{1}{2}\sqrt{2}$	10	1	$\begin{pmatrix} a & b \\ b & a \end{pmatrix}$	45	125,000
3	1	0	100	10	$\begin{pmatrix} a & 0 \\ 0 & b \end{pmatrix}$	0	125,000
4	$\frac{1}{2}\sqrt{2}$	$-\frac{1}{2}\sqrt{2}$	100	10	$\begin{pmatrix} a & b \\ b & a \end{pmatrix}$	45	125,000
5	0.6	−0.8	10	1	$\begin{pmatrix} a & c \\ c & b \end{pmatrix}$	53	125,000

as by the dispersivity values. The anisotropy ratio here is in each test case equal to 10 : 1. For all test cases, an overlap ratio ($\frac{h}{\varepsilon}$) of 0.9 was selected. Remeshing every one or two time steps when necessary and appropriately selecting the time step for the integration of the particle trajectories ensures that on average this ratio is observed in our simulations.

3.1.1. *The Influence of the Core Size (ε)*

The error of the approximation of the diffusion–dispersion operator by a smooth integral operator is associated with the core size of the regularization function of the particles. Since the overlap ratio is kept constant, the variation of the core size is also connected to the interparticle spacing and thus to the number of particles. The influence of the core size is evaluated by examining cases 1, 2, and 5 (with a second order cutoff function) which are distinguished by the form of the dispersion tensor **D**. In this way the influence of the various forms of the dispersion tensor can be examined too.

Diminishing the core size and thus the interparticle spacing means obtaining a higher resolution simulation. The errors of all test cases can be consistently reduced by reducing the core radius of the particles (Fig. 1). The method produces the same behaviour irrespective of the character of the dispersion matrix. The reason is that our method does not use a structured grid such as in finite differences and therefore shows no grid anisotropy.

3.1.2. *The Influence of the Time Step Size*

In order to assess the effect of the time step we examine cases 1, 3, and 4 by varying the size of the time step and the order of the cutoff function. Figure 2 shows that the results of case 1 are stable for a time step which can be about 10 times higher than for cases 3 and 4.

The restriction found on the time step size with test case 4 is

$$\Delta t \leq c \frac{\varepsilon^2}{D_{xx} + D_{yy}},$$

where ε is the core size of the regularization function of the particles and $c \approx 2.5$ for a second order cutoff function (Eq. (20); Fig. 2b), $c \approx 1.2$ for a fourth order cutoff function (Eq. (21); Fig. 3), and $c \approx 0.7$ for a sixth order cutoff function (Eq. (22); Fig. 3), similar to

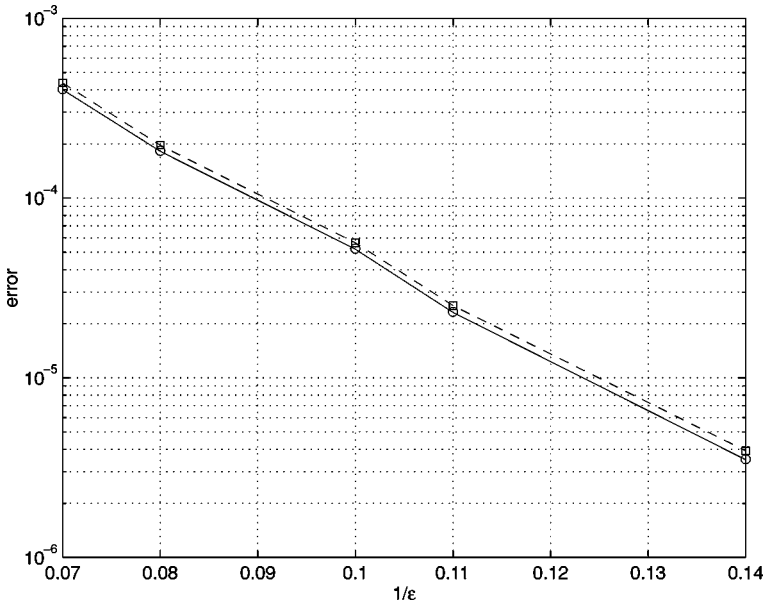

FIG. 1. Error (I) of the numerical solution in comparison with the analytical solution with varying core size; case 1 (dashed line, squares), case 2 (solid line), case 5 (circles).

but slightly weaker than the Neumann condition for explicit finite difference methods:

$$\triangle t \leq 0.5 \frac{\triangle x^2}{D_{xx} + D_{yy}}. \tag{29}$$

The restrictions on the time step size become more pronounced using a higher order cutoff function (Fig. 3). Further tests with various anisotropy ratios showed the same time step restrictions. Although subject to a severe time step size constraint, the use of an explicit time stepping procedure does facilitate the parallelization of the method.

Degond and Mas-Gallic, in their original papers [7, 8], conducted a rigorous stability analysis of the proposed method. A stability analysis here is further complicated by the remeshing which periodically maps the particles onto a regular grid. It has been shown by Cottet [4] that the PSE is equivalent to a finite difference method when the particles occupy regular grid nodes. When remeshing is implemented this analysis is pertinent. The results presented in this work reflect this property although the stability constants have been found empirically through the present computations.

3.2. Examination of Various Anisotropy Ratios and the Influence of Remeshing

In this section we present simulations with various anisotropy ratios. The parameters used for the simulations are summarized in Table II. The core size (ε) of the particles' regularization function is between 10 and 11 m and the width of the Gaussian input (ε_{src}) is about four times larger than the core size of one particle's regularization function. N_{rem} denotes the remeshing frequency (time steps per remeshing) and M_{in} the input of pollutant mass. Note that in the following simulations remeshing is not really needed as the velocity field is constant. A second order cutoff function $\bar{\Theta}$ (Eq. 20) was used for each case except

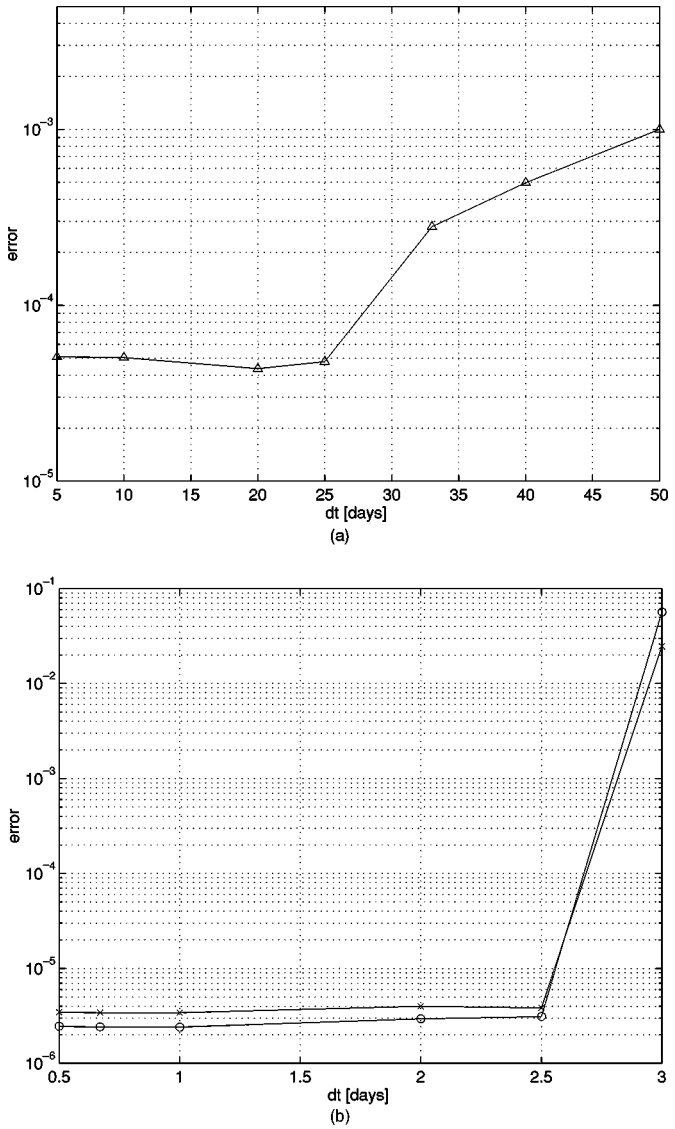

FIG. 2. Error (I) of the numerical solution in comparison with the analytical solution while varying the size of the time step. Numerical solutions were conducted with a second order cutoff function and a core size of $\varepsilon = 11$ m. (a) Case 1 (solid line, triangle); (b) case 3 (solid line, $\times$-marks); and case 4 (solid line, circles).

for case 8 where we additionally used a fourth order cutoff function (Eq. 21). An overlap ratio ($\frac{h}{\varepsilon}$) of 0.9 was used for each test case.

3.2.1. *Purely Advective Case*

The breakthrough curves (Fig. 4) show a remarkable agreement between the numerical and the analytical calculations. The calculations were conducted without any dispersion ($\alpha_L = 0$ and $\alpha_T = 0$). The run took about 8 CPU sec with a particle number of 1800. The relative error at the observation point X(25/$-$25) between the exact and the numerical simulation with a remeshing frequency (N_{rem}) of 1 per time step is zero at the beginning,

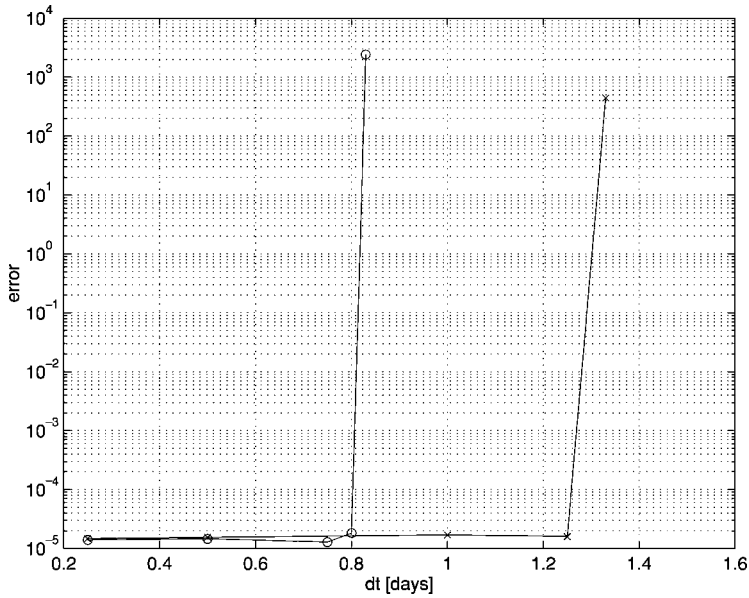

FIG. 3. Error (I) of the numerical solution (with a core size of $\varepsilon = 11$ m) in comparison with the analytical solution while varying the size of the time step. Case 4 with a fourth order cutoff function (solid line, $\times$-marks) and with a sixth order cutoff function (solid line, circles).

fluctuates between -0.1 and 0.1% and increases up to -0.3% at the end of the simulation (Fig. 5). That indicates that the concentrations at the tip and the tail of the plume are higher in the numerical case. This may be attributed to the numerical error introduced by remeshing. The relative error of the maximum concentration of the plume at time t (Fig. 6) increases slowly from 0 to 0.18%. The maximum concentration of the numerical simulation is always lower than that of the exact solution. The relative errors of the simulations without remeshing are in both cases constant and more than two to three orders of magnitude smaller than the errors occurring with a remeshing at every time step. The continuous transition to the limit $\alpha_L \to 0, \alpha_T \to 0$ is a remarkable feature of particle methods which cannot be as easily obtained by methods with a fixed grid.

3.2.2. *Moderately Anisotropic Case*

Figure 7 represents the temporal development of the plumes of both the numerical (top) and the analytical (bottom) calculations at 200, 500, and 1000 days. The parameters used

TABLE II
Parameters Used for the Examination of Different Anisotropy Ratios

Case	u_x [m/d]	u_y [m/d]	α_L [m]	α_T [m]	dt [d]	ε [m]	N_{rem} [$-$]	ε_{src} [m]	M_{in} [g]	t_{max} [d]
6a	$\frac{1}{2}\sqrt{2}$	$-\frac{1}{2}\sqrt{2}$	0	0	10	11	1	44	10^6	300
6b	$\frac{1}{2}\sqrt{2}$	$-\frac{1}{2}\sqrt{2}$	0	0	10	11	∞	44	10^6	300
7a	$\frac{1}{2}\sqrt{2}$	$-\frac{1}{2}\sqrt{2}$	100	10	2	11	2	44	10^6	1000
7b	$\frac{1}{2}\sqrt{2}$	$-\frac{1}{2}\sqrt{2}$	100	10	2	11	∞	44	10^6	1000
8	$\frac{1}{2}\sqrt{2}$	$-\frac{1}{2}\sqrt{2}$	100	1	2	10	2	44	10^6	1000

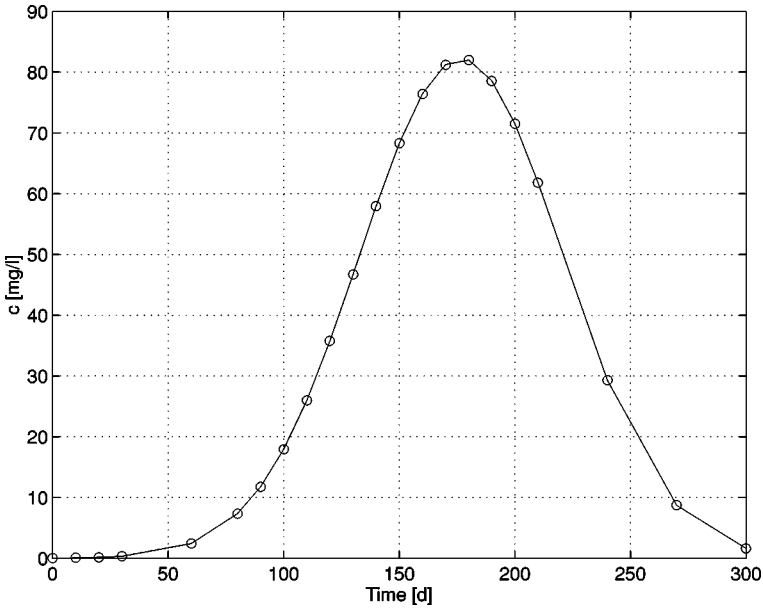

FIG. 4. Breakthrough curves of the numerical (circles) and analytical (solid line) solutions at point X(25/−25) without dispersion (case 6a with $N_{rem} = 1$). The instantaneous source is at point (−100/100) m.

for the simulation are shown in Table II (case 7a with $\alpha_L = 100$ m and $\alpha_T = 10$ m). The number of particles increased linearly with an average particle number of 25,000 and a maximum number of 50,000 (with a computational expense of 4 CPU min).

The breakthrough curves (Fig. 8) and the curves of the maximum concentrations (Fig. 9) confirm the good agreement between the simulations and the analytical results. The relative

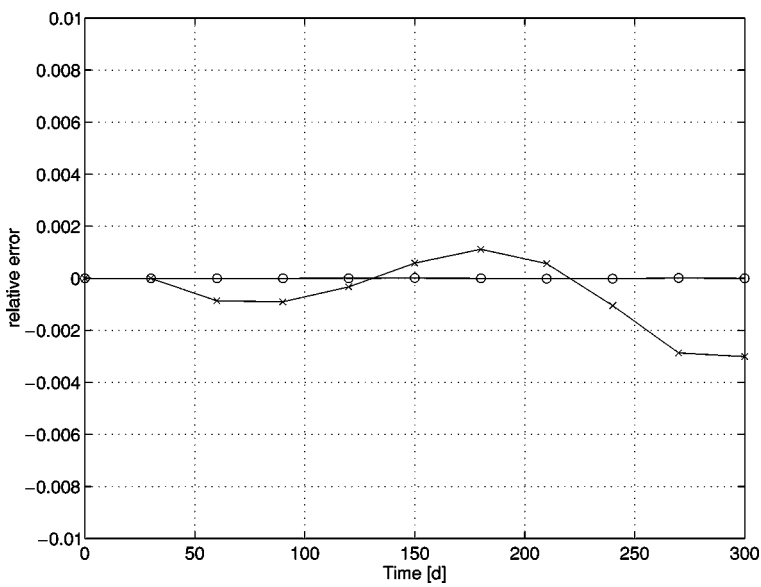

FIG. 5. Relative error (II) at point X(25/−25), with $\alpha_L = 0$ m and $\alpha_T = 0$ m, with a remeshing frequency of 1 (case 6a, solid line, x-marks) and without remeshing (case 6b, solid line, circles).

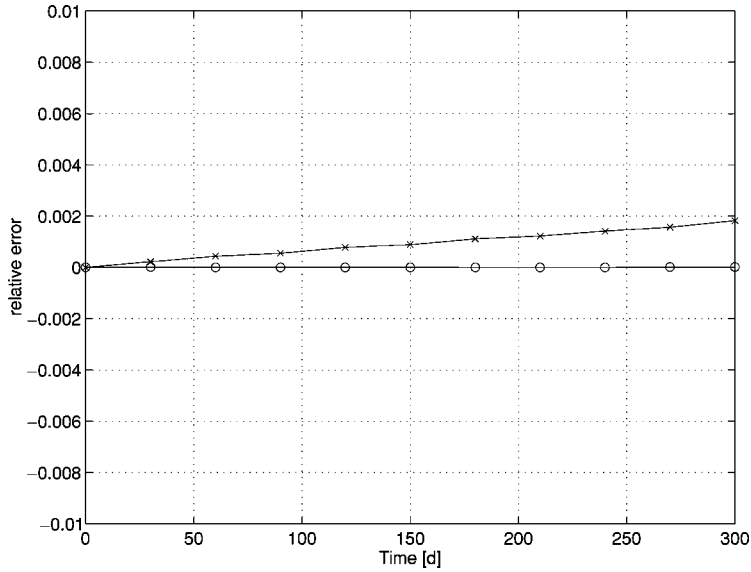

FIG. 6. Relative error (II) of the maximum concentration of the plume versus time t, with $\alpha_L = 0$ m and $\alpha_T = 0$ m, with a remeshing frequency of 1 (case 6a, solid line, $\times$-marks) and without remeshing (case 6b, solid line, circles).

error at the observation point X(20/−20) is more significant at the tip of the plume. It increases up to the time (t = 120 days) the maximum of the plume has moved across the observation point, and then decreases from about 0.5 to about 0.3%. The relative error of the maximum concentration increases up to 0.7% right at the beginning (t = 20 days) and

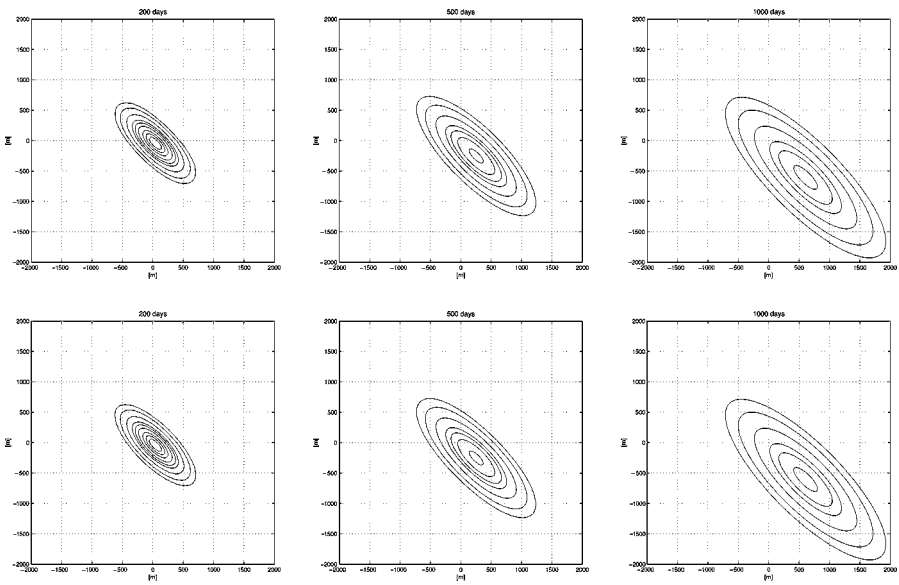

FIG. 7. Comparison between the solutions of the numerical method with $N_{rem} = 2$ (top) and the analytical solution (bottom) for case 7a with $\alpha_L = 100$ m and $\alpha_T = 10$ m at 200, 500, and 1000 days due to an instantaneous injection at point (−100/100). The contour lines represent the following concentrations c = 0.001, 0.01, 0.1, 0.5, 1.0, 2.0, 4.0, 6.0, and 8.0 [mg/l].

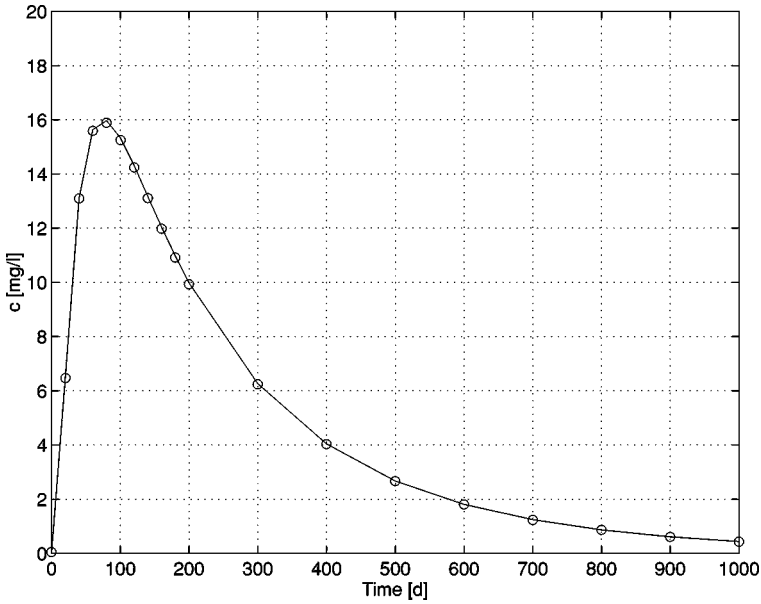

FIG. 8. Breakthrough curves of the numerical (circles) and analytical (solid line) solutions at point X(20/−20) with $\alpha_L = 100$ m and $\alpha_T = 10$ m (case 7a). The instantaneous source is located at point (−100/100).

decreases evenly to less than 0.2% at the end of the simulation time. The error is thus more significant at the earlier stage of the simulation.

In contrast to the simulations without dispersion (Section 3.2.1), the relative error is about the same here regardless of whether the simulations are conducted with a remeshing at every second time step (Fig. 10) or without any remeshing at all (Fig. 11). This signifies

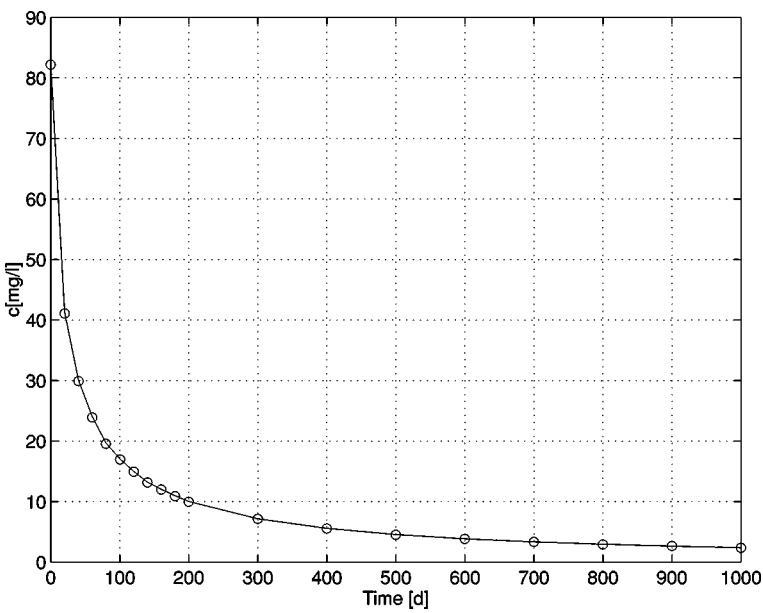

FIG. 9. Maximum concentration of the plume at time t of the numerical (circles) and the analytical (solid line) solutions with $\alpha_L = 100$ m and $\alpha_T = 10$ m (case 7a).

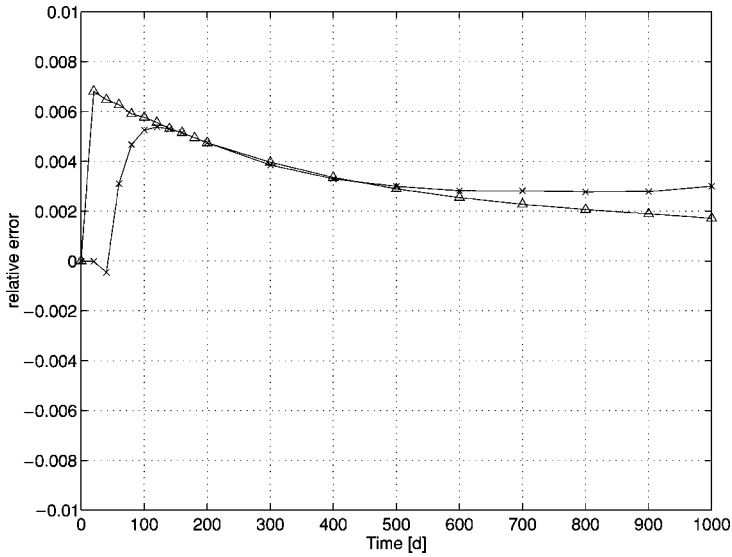

FIG. 10. Relative error (II) of the maximum concentration of the plume (solid line, triangles) and of concentrations at point X(20/−20) (solid line, ×-marks) versus time t, with $\alpha_L = 100$ m and $\alpha_T = 10$ m and a remeshing at every second time step ($N_{rem} = 2$), (case 7a).

that the error of the remeshing is much less significant than the error introduced by the approximation of the dispersion operator (Section 2.2.1).

3.2.3. *Strongly Anisotropic Case*

Finally, we consider simulations with high ratios of the longitudinal and transversal dispersivities. Anisotropy ratios of $\alpha_L : \alpha_T$ of 100 : 1 to 1000 : 1 are relevant for practical

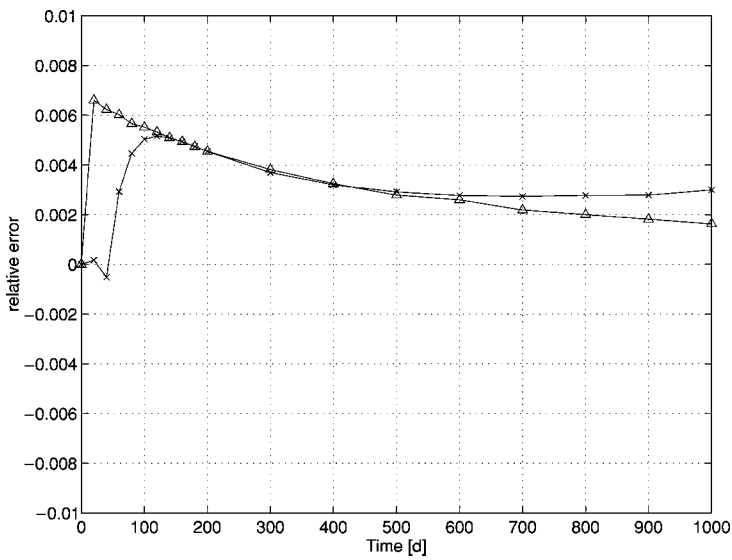

FIG. 11. Relative error (II) of the maximum concentration of the plume (solid line, triangles) and of concentrations at point X(20/−20) (solid line, ×-marks) versus time t, with $\alpha_L = 100$ m and $\alpha_T = 10$ m and no remeshing, (case 7b).

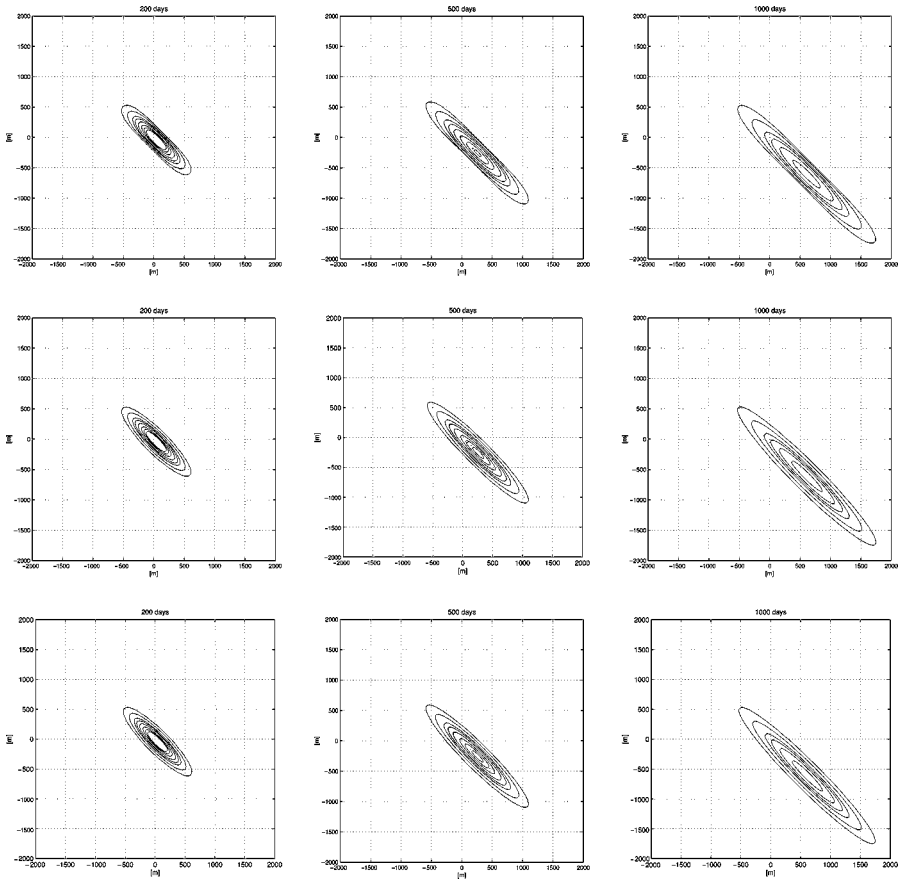

FIG. 12. Comparison between the solution of the numerical method with a second order cutoff function (top), and with a fourth order cutoff function (middle), and the analytical solution (bottom) for $\alpha_L = 100$ m and $\alpha_T = 1$ m at 200, 500, and 1000 days due to an instantaneous injection at point $(-100/100)$ (case 8). The contour lines represent the concentrations c = 0.01, 0.1, 0.5, 1.0, 2.0, 4.0, 6.0, and 8.0 [mg/l].

applications in groundwater studies and pose problems for finite difference, finite element, and characteristic methods. In Fig. 12 we present the contour plots of the numerical simulations of case 8 ($\alpha_L = 100$ m, $\alpha_T = 1$ m). The simulation was performed with an average number of 17,000 particles and a maximum number of 30,000 (with a computational cost of 3 CPU min). Comparing the results of the numerical simulations with a second order cutoff function with the exact solution (top and bottom row in Fig. 12), one may observe oscillations in the transversal direction and a broadening of the tip and the tail of the plume in the numerical simulations. Unlike other cases, here negative concentration values up to almost 1% of the maximum concentration were generated. The numerical simulations with a fourth order cutoff function (Fig. 12, middle row), however, do not show these numerical instabilities and the contour plots match the exact ones well. Negative concentration values never exceeded 0.0003% of the maximum concentration. Figures 13 and 14 verify the remarkable agreement between the numerical calculations with a fourth order cutoff function and the exact calculations. The numerical simulations with a second order cutoff function show lower concentrations at both the observation point X(20/−20) and the maximum concentration at time t. In the case of numerical simulations with a second order cutoff

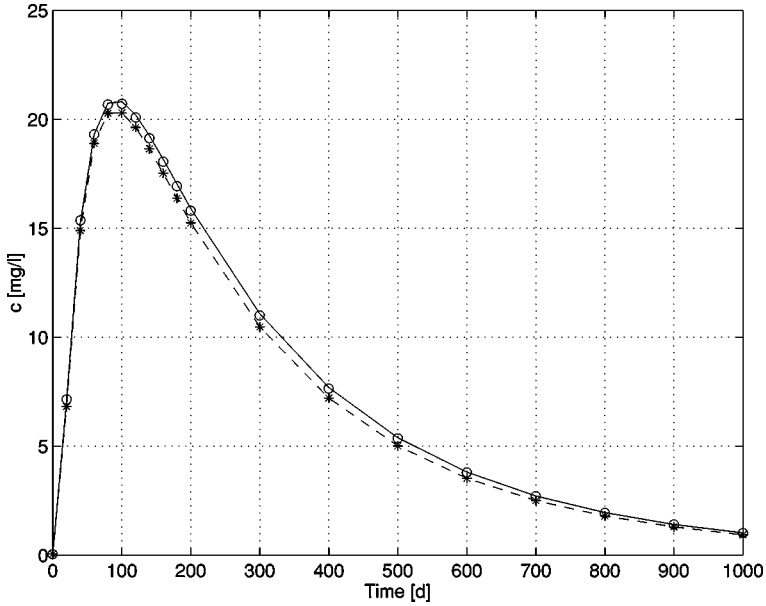

FIG. 13. Breakthrough curves of the numerical solution (with a second and a fourth order cutoff function) and the analytical solution at point X(20/−20) with $\alpha_L = 100$ m and $\alpha_T = 1$ m (case 8). The instantaneous source is located at point (−100/100). Analytical solution (solid line), and numerical solution with a second order cutoff function (dashed line, stars) and with a fourth order cutoff function (circles).

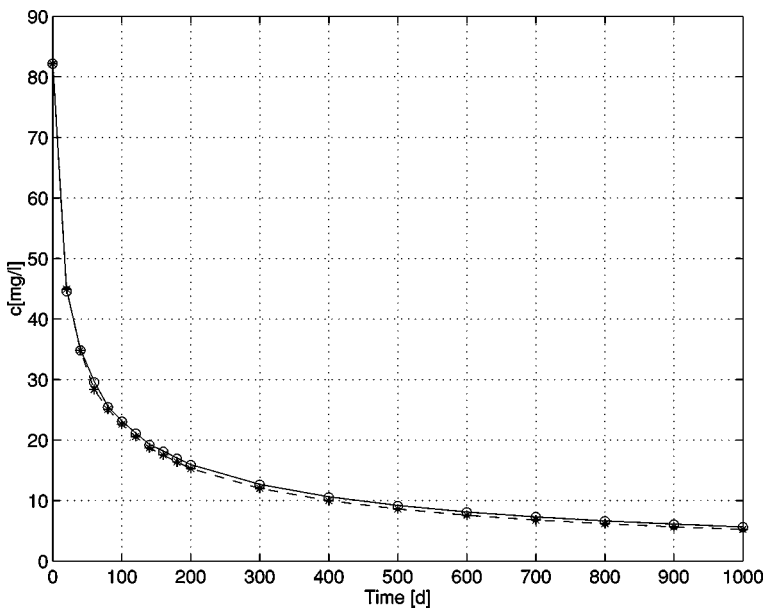

FIG. 14. Maximum concentration of the plume at time t of the numerical solution (with a second and fourth order cutoff function) and the analytical solution with $\alpha_L = 100$ m and $\alpha_T = 1$ m (case 8). Analytical solution (solid line), and numerical solution with a second order cutoff function (dashed line, stars) and a fourth order cutoff function (circles).

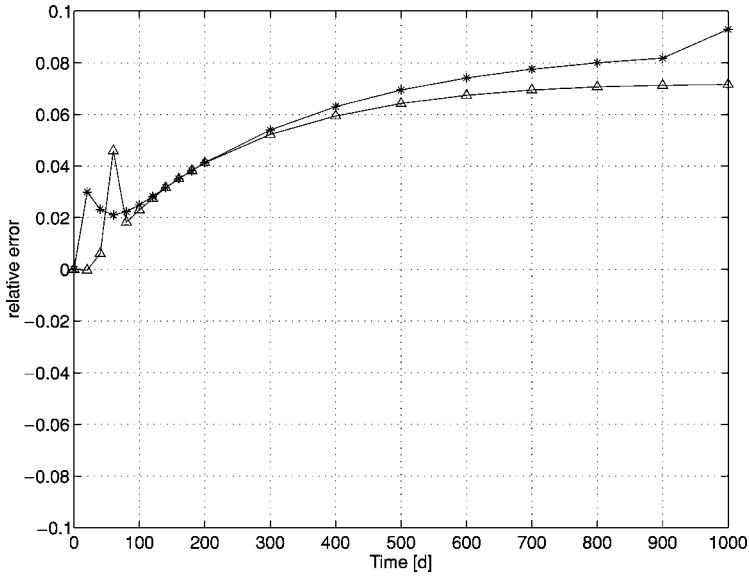

FIG. 15. Relative error (II) of the maximum concentration of the plume (solid line, triangles) and of concentrations at point X(20/−20) (solid line, stars) versus time t, with $\alpha_L = 100$ m and $\alpha_T = 1$ m and a second order cutoff function (case 8).

function the relative error of concentrations at the observation point X(20/−20) and in the maximum increases up to 9%, respectively 7% at t = 1000 days (Fig. 15). Simulations with a fourth order cutoff function show an almost constant error of 0.25% at the observation point and 0.35% at the point of maximum concentration (Fig. 16). The most significant discrepancy is observed at the tip of the plume resp. at the earlier stage of the simulation.

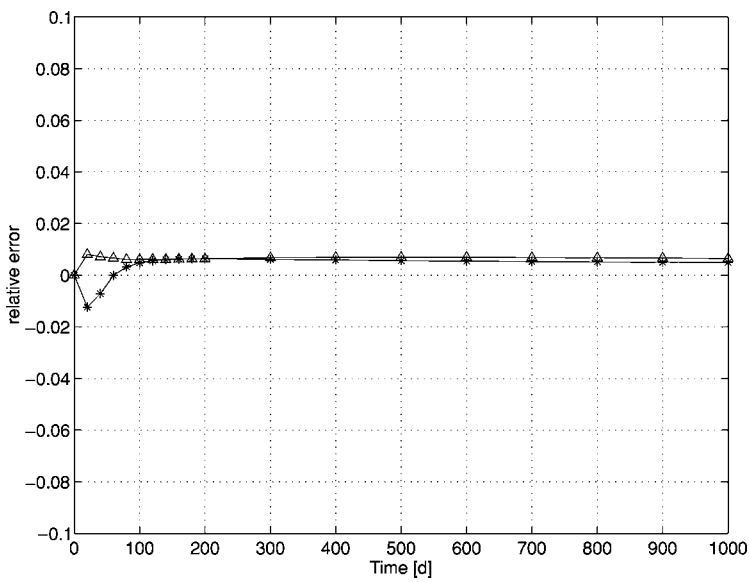

FIG. 16. Relative error (II) of the maximum concentration of the plume (solid line, triangles) and of concentrations at point X(20/−20) (solid line, stars) versus time t, with $\alpha_L = 100$ m and $\alpha_T = 1$ m and a fourth order cutoff function (case 8).

Taking a higher than fourth order cutoff function (e.g., sixth order) does not further change the results qualitatively (see Section 3.4). Since we saw in Section 3.2.2 that good results with a second order cutoff function could be obtained for an anisotropy ratio of 10 : 1, the numerical difficulties here derive from the high anisotropy ratio of 100 : 1.

3.3. Comparison with a Finite Difference Model

In order to compare the results of our method with another numerical method, case 8 has been modelled with 'MT3DMS,' a public domain finite difference simulation code [24]. The advection term is discretized with explicit upstream finite differences. The model area is 2000×2000 m with a cell size of 10×10 m and a source dimension of 50×50 m. A time step of 1 day was chosen. Note that the time stepping method (explicit) and the discretization in space and time $\triangle x$, $\triangle t$ are comparable to those in case 8. However, since the initial conditions are different in this FD model (input of a source with a rectangular shape), the results of the two methods can only be compared qualitatively. Figure 17 presents

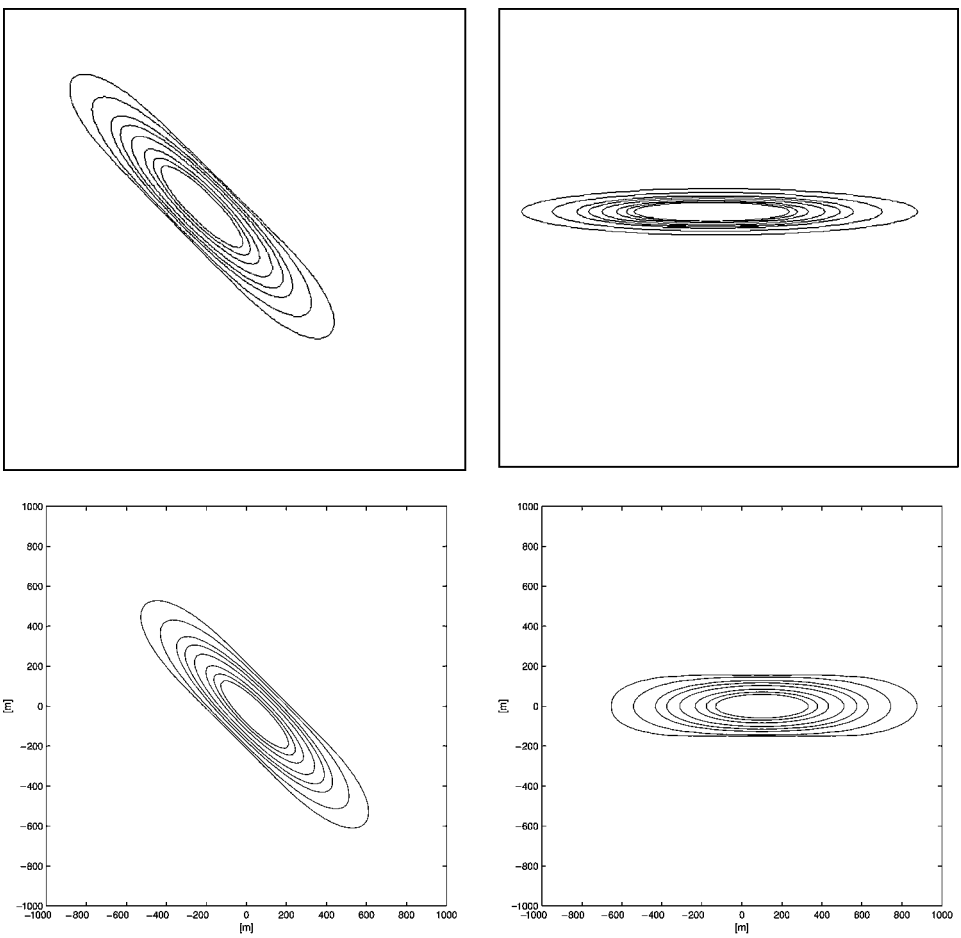

FIG. 17. Contour plots performed with 'MT3DMS' (top) and the particle code (bottom), at 200 days with $\alpha_L = 100$ m and $\alpha_T = 1$ m. The flow field is diagonal to the x-axis (left) and parallel to the x-axis (right). The model domain is 2000 m $\times$ 2000 m. The contour lines represent the concentrations c = 0.01, 0.1, 0.5, 1.0, 2.0, 4.0, 6.0, and 8.0 [mg/l].

the results after 200 days with a flow direction diagonal (left) and parallel (right) to the x-axis for both the finite difference and the particle method. By comparing the results obtained with the finite difference method one may observe in the left half of the figure (with a diagonal flow direction) a broadening of the plume in the transversal direction and also a shortening of the plume in the longitudinal direction. In addition one can also observe numerical oscillations in the transversal direction. The so-called angular–numerical dispersion (grid anisotropy) is well known in FD models and stems from the fact that the true direction of the pulse cannot be represented on the discrete grid, as mass transport is only approximated between direct neighbour cells [20]. If the grid is not aligned with the flow direction, its anisotropy interferes with the anisotropy of the dispersion tensor. In [11] it is shown that the dispersive part of the operator already causes spurious widening of a plume or cloud, which is especially disturbing for slender plumes. One might argue that in the test case used here the transformation to an isotropic case and to a grid that is aligned with the flow direction is possible since the flow is parallel. But in general, flows are nonuniform and streamlines are curved due to wells, recharge, and discharge points; a FD grid—contrary to our method—cannot be aligned with the flow in all places simultaneously nor does a transformation exist that makes the problem isotropic. The results obtained with the particle method with a second order cutoff function indicate numerical instabilities in both cases—with a flow direction diagonal to the x-axis and parallel to the x-axis. Note that we use here a second order cutoff function for comparison reasons with the FD code. The numerical instabilities disappear when using a fourth or higher order cutoff function (see Section 3.2.3).

The simulations with the FD model show numerical dispersion and oscillations only in the case in which the flow direction is not aligned with a coordinate axis, while our method yields results which are independent of the flow direction.

Finally, we examined the diagonal case shown in Fig. 17 with both methods (finite difference and particle method) by varying the number of gridpoints and particles, respectively. The cell size $\triangle x, \triangle y$ and the interparticle spacing are 10, 20, and 50 m, respectively. The simulations with the particle code are performed with a second order cutoff function. The relative errors of the maximum concentration are depicted in Fig. 18. With both methods the error decreases with the number of gridpoints or particles. With the particle code many fewer particles than gridpoints are needed to obtain the same accuracy. The reason is that for the particle code, particles are only needed at locations of the pollutant plume, whereas in finite differences the entire domain has to be discretized consistently. The elapsed CPU time is shown in Fig. 19. For the simulations performed with a cell size or interparticle spacing of 20 and 50 m, both methods needed about the same CPU time. In the case with the highest accuracy, the particle code is about 10 times faster than the FD code.

3.4. Examination of Cutoff Functions of Different Order

Figure 20 shows the accuracy of the second, fourth, and sixth order cutoff functions, examining test cases 7a and 8 at t $=$ 200 days. The error (I) of case 8 (with a high anisotropy ratio of 100 : 1) is more than two orders of magnitude smaller with a fourth or sixth order cutoff function than with a second order cutoff function. The accuracy of the results of case 7a (with an anisotropy ratio of 10 : 1), however, does not change significantly with the order of the cutoff function. The drawback of the use of a higher order cutoff function is the more restrictive time step constraint (see Section 3.1.2).

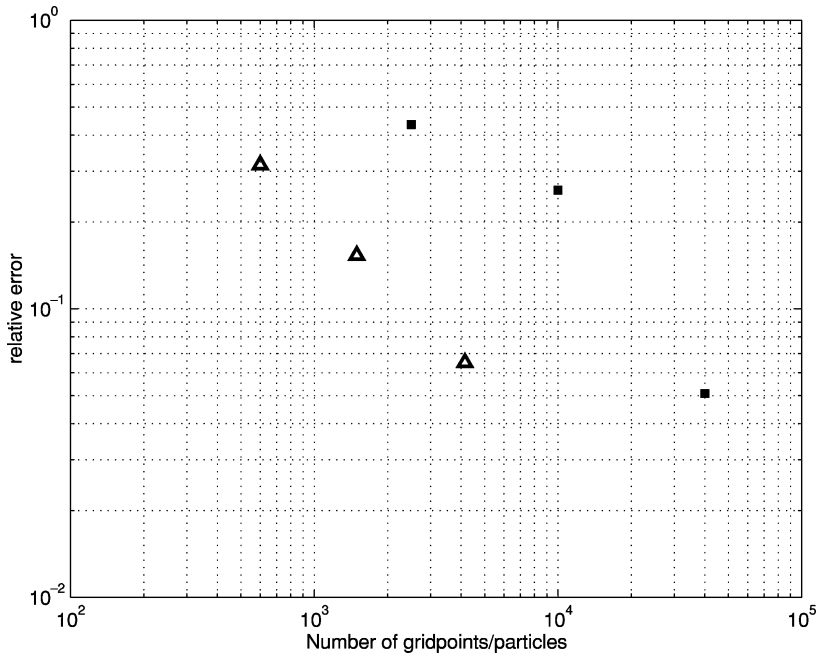

FIG. 18. Relative error (II) of the maximum concentration at 200 days versus the number of gridpoints and particles, respectively. The squares represent the results conducted with the FD code; the triangles represent the results conducted with the particle code. The flow field is diagonal, with $\alpha_L = 100$ m and $\alpha_T = 1$ m (see Fig. 17).

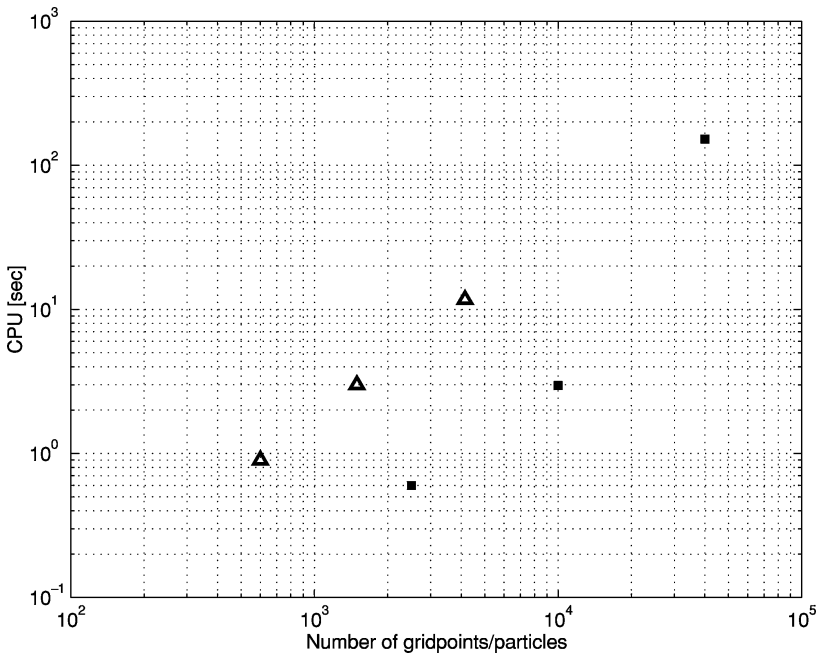

FIG. 19. Elapsed CPU time in seconds versus number of gridpoints (FD code, squares) and number of particles (particle code, triangles).

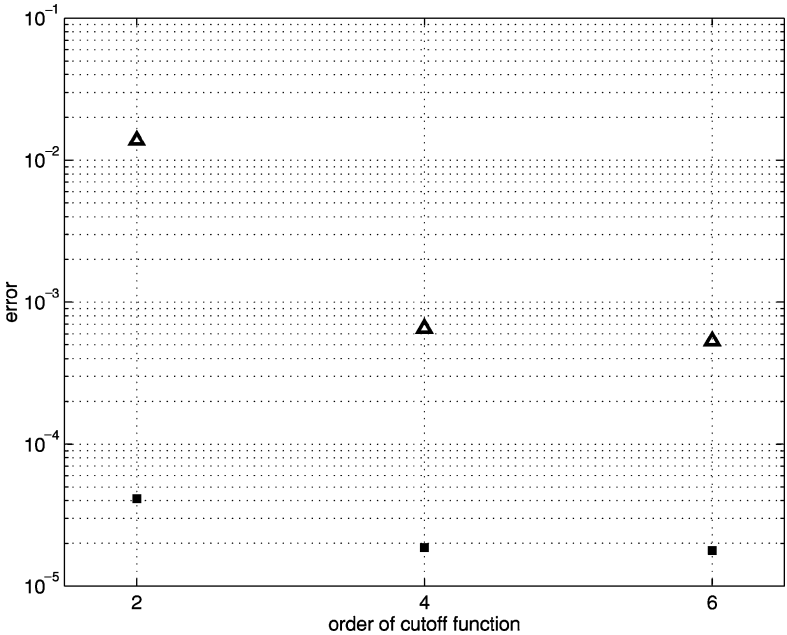

FIG. 20. Error (I) of the numerical solution (case 7a and case 8) at t = 200 days in comparison to the analytical solution and to varying orders of the cutoff function (second, fourth, and sixth order cutoff function). Case 7a with $\alpha_L = 100$ m and $\alpha_T = 10$ m (squares); case 8 with $\alpha_L = 100$ m and $\alpha_T = 1$ m (triangles).

4. NUMERICAL RESULTS WITH A NONCONSTANT VELOCITY FIELD

In this section we present the results of simulations with a nonconstant velocity field, a case where no analytical solutions with which to compare exist. For this purpose the code was extended to deal with a spatially variable velocity field. The velocity field was implemented by the analytical expression of a velocity field which is the superposition of a constant flow field with the flow field induced by pointlike sources (infiltration wells) and sinks (pumping wells),

$$\mathbf{v}(\mathbf{x}) = \mathbf{v}_o + \sum_i \frac{1}{2\pi} \frac{Q_i}{|\mathbf{x} - \mathbf{y}_i|}, \tag{30}$$

where $\mathbf{v}_o$ describes the constant flow field, Q_i is the pumping rate of well i, $\mathbf{y}_i$ is the location of the i-th well, and $\mathbf{v}(\mathbf{x})$ is the value of the (combined) velocity field at point $\mathbf{x}$. The aquifer is assumed to extend to infinity. Note that the nonconstant velocity field implies a spatially varying dispersion tensor (see Section 2.2.2).

We consider one infiltration well located at x = 0 m, y = 0 m and two pumping wells located at x = −50 m, y = 0 m and x = −20 m, y = −60 m, respectively, embedded in a constant flow field with $u_x = 0.2$ [m/day] and $u_y = -0.2$ [m/day]. The flow rate of the infiltration well is Q = 30 [m^3/day] and that of the pumping wells Q = − 20 [m^3/day]. This type of flow field appears in applications of hydraulic remediation measures where the natural flow is modified to direct a plume, or remove a plume, or prevent a plume from reaching a downstream water pumping well. In the example, the plume originates from a permanent source of pollutant mass located at x = −20 m, y = 40 m. The simulation was

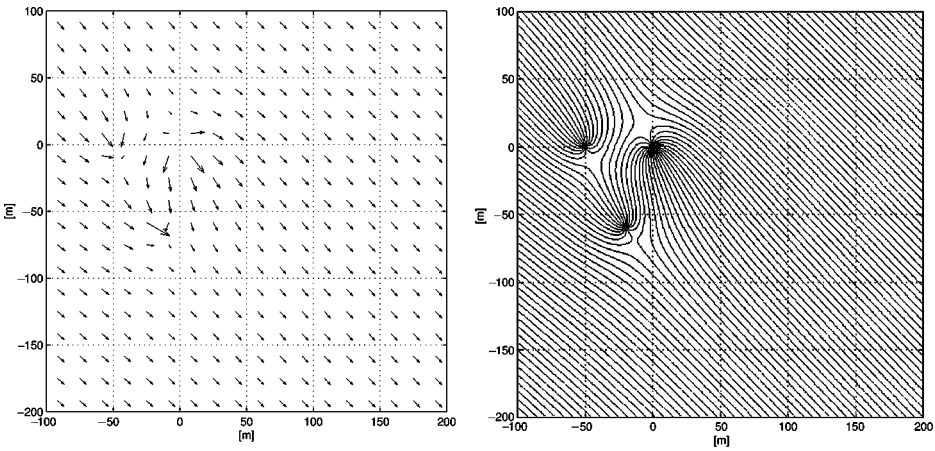

FIG. 21. Velocity field visualized as velocity vectors (left) and streamlines (right).

performed with an average particle number of 14,000 and a maximum number of 28,000, and it took about 8 CPU min.

The velocity field visualized by velocity vectors as well as streamlines is depicted in Fig. 21. Particles which enter a sink are discharged. Figure 22 shows the temporal development of the plume with a remeshing frequency of 5. It moves along the streamlines and the sharp fronts can be well simulated. For comparison reasons, Fig. 23 shows the results of simulations conducted with a remeshing frequency of 40. Since the velocity field is not constant anymore, simulations with too large a remeshing interval lead to unstable results.

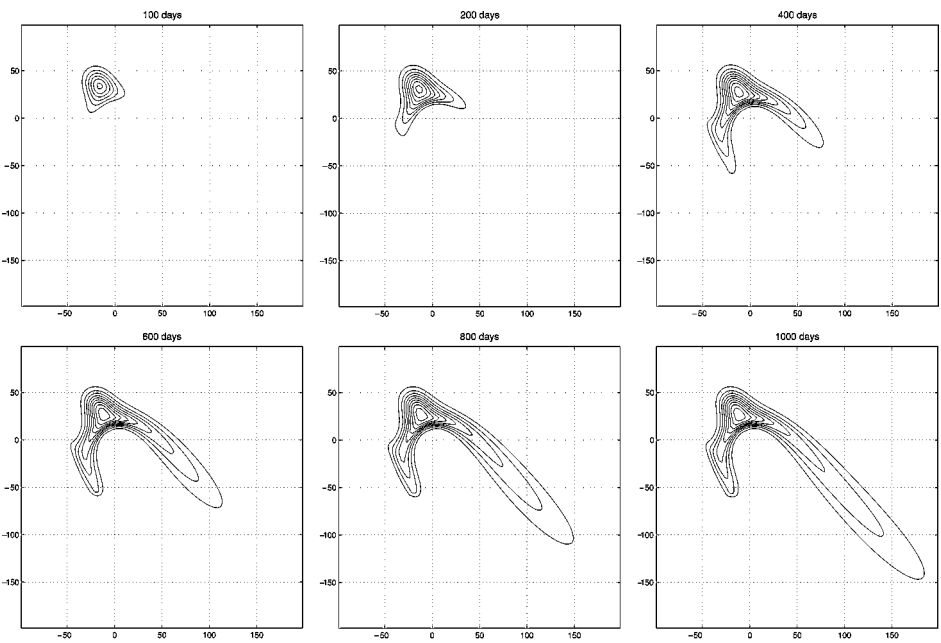

FIG. 22. Temporal development of a permanent injection at point X(−20/40) with a remeshing frequency of 5 at 100, 200, 400, 600, 800, and 1000 days. The area is 300 × 300 m. The contour lines represent the concentrations c = 100, 200, 300, 400, 500, 600, 700, 800, and 900 [mg/l].

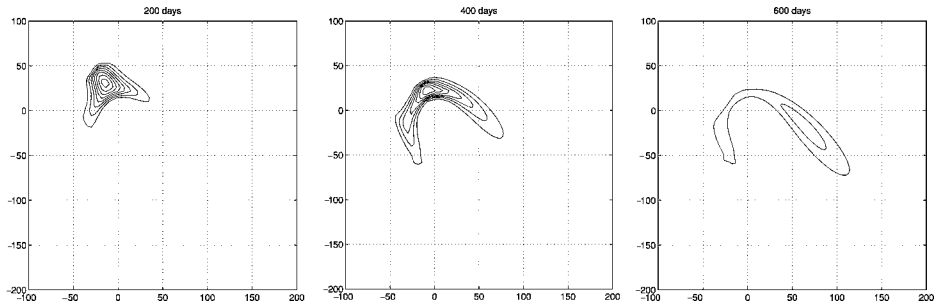

FIG. 23. Temporal development of a permanent injection at point X(−20/40) with a remeshing frequency of 40 at 200, 400, and 600 days. The contour lines represent the concentrations c = 100, 200, 300, 400, 500, 600, 700, and 800 [mg/l].

Locally, particles cease to overlap, thus violating the convergence criterion requiring that particles must overlap at all times (Section 2.3).

5. CONCLUSIONS

A Lagrangian scheme has been presented for the two-dimensional simulation of passive pollutant transport in a porous medium. The anisotropic extension of the particle strength exchange scheme has been implemented to describe the diffusive–dispersive process. A validation study has been conducted in which the effect of the time step size, the core size of the regularization function of the particles, and various forms of the dispersion tensor have been studied. Furthermore, various cutoff functions, anisotropy ratios, and remeshing frequencies have been examined. We have compared the numerical results with the analytical solution of a Gaussian shaped pollutant injection into a constant external velocity field.

In summary, the benchmarks prove the presented numerical method to be accurate and stable even in the limiting cases of vanishing diffusion–dispersion and high anisotropy ratios, both of which are of great practical relevance in groundwater applications. The simulation of a permanent pollutant injection into a more complex flow topology with sources and sinks added to the constant flow field shows that the method is very capable of dealing with spatially variable diffusion–dispersion tensors.

From the test cases in the validation study we find the following results. The method shows no grid-induced anisotropy. Very good results are obtained for the purely advective ($\alpha_L = 0, \alpha_T = 0$) and the moderately anisotropic ($\alpha_L : \alpha_T = 10 : 1$) cases. Simulations with a high anisotropy ratio ($\alpha_L : \alpha_T = 100 : 1$) require the use of a higher than second order cutoff function (fourth or sixth order) to obtain good results. Using a fourth or a sixth order cutoff function increases the accuracy significantly only in the strongly anisotropic case. The drawback of the use of a higher order cutoff function is, however, the more restrictive time step constraint. The errors introduced by occasionally remeshing the particles' locations are less significant than the errors introduced by the approximation of the differential diffusion–dispersion operator by an integral operator.

The results of the simulations using the PSE scheme with the anisotropic extension demonstrate that PSE can accurately handle even high anisotropy ratios. In the context of groundwater pollution transport modelling the presented method proves to be a very accurate and interesting alternative to other particle methods such as random walk or the method of characteristics.

ACKNOWLEDGMENTS

We acknowledge many helpful discussions with Dr. J. H. Walther. This project was funded by the Swiss Federal Institute of Technology Zürich (ETHZ).

REFERENCES

1. M. B. Abbott, *An Introduction to the Method of Characteristics* (American Elsevier, New York, 1966).
2. A. J. Chorin, Numerical study of slightly viscous flow, *J. Fluid Mech.* **57**, 785 (1973).
3. G.-H. Cottet, *Analyse Numérique des Méthodes Particulaires pour Certains Problèmes Nonlinéaires*, thèse d'État (Université Pierre et Marie Curie, 1987).
4. G.-H. Cottet, A particle-grid superposition method for the Navier–Stokes equations, *J. Comput. Phys.* **89**, 301 (1990).
5. G.-H. Cottet, Artificial viscosity models for vortex and particle methods, *J. Comput. Phys.* **127**, 299 (1996).
6. G.-H. Cottet and P. Koumoutsakos, *Vortex Methods: Theory and Practice* (Cambridge Univ. Press, Cambridge, UK, 1999).
7. P. Degond and S. Mas-Gallic, The weighted particle method for convection-diffusion equations, Part I: The case of isotropic viscosity, *Math. Comput.* **53**, 485 (1989).
8. P. Degond and S. Mas-Gallic, The weighted particle method for convection-diffusion equations, Part 2: The anisotropic case, *Math. Comput.* **53**, 509 (1989).
9. L. Greengard and V. Rohklin, A fast algorithm for particle simulations, *J. Comput. Phys.* **73**, 325 (1987).
10. S. Huberson, *Modélisation Asymptotique et Numérique de Noyaux Tourbillonaires Enroulés*, thèse d'État (Université Paris VI, 1986).
11. W. Kinzelbach and E. Frind, Accuracy criteria for advection–dispersion models, in *Finite Elements in Water Resources, Proceedings of the 6th International Conference* (Springer Verlag, Berlin, 1986), Vol. 489.
12. W. Kinzelbach, The random walk method in pollutant transport simulations, in *Groundwater Flow and Quality Modelling*, edited by E. Custodia, A. Gurgui, and J. P. Lobo Ferreira, NATO ASI series C. Mathematical and Physical Sciences (Reidel, Norwell, MA, 1988), Vol. 224, p. 227.
13. W. Kinzelbach, *Numerische Methoden zur Modellierung des Transportes von Schadstoffen im Grundwasser* (Oldenbourg, Munich, 1992).
14. P. Koumoutsakos, *Direct Numerical Simulations of Unsteady Separated Flows Using Vortex Methods*, Ph.D. thesis (California Institute of Technology, 1993).
15. P. Koumoutsakos and A. Leonard, High resolution simulations of the flow around an impulsively started cylinder using vortex methods, *J. Fluid Mech.* **296**, 1 (1995).
16. P. Koumoutsakos, Inviscid axisymmetrization of an elliptical vortex, *J. Comput. Phys.* **138**, 821 (1997).
17. S. Mas-Gallic, *Contribution à l'Analyse Numérique des Méthodes Particulaires*, thèse d'État (Université Paris VI, 1987).
18. A. E. Scheidegger, General theory of dispersion in porous media, *J. Geophys. Res.* **66**, 3273 (1961).
19. P.-A. Raviart, *Méthodes Particulaires*, Lecture notes, Ecole d'été d'analyse numérique, Centre d'Étude du Bréau-sans-nappe, France, 1987 (unpublished).
20. K. Spitz and J. Moreno, *A Practical Guide to Groundwater and Solute Transport Modeling* (Wiley, New York, 1996).
21. G. Uffink, *Analysis of Dispersion by Random Walk Method*, Ph.D. thesis (Delft University, 1990).
22. G. S. Winckelmans, *Topics in Vortex Methods for the Computation of Three- and Two-Dimensional Incompressible Unsteady Flows*, Ph.D. thesis (California Institute of Technology, 1989).
23. G. S. Winckelmans and A. Leonard, Contributions to vortex particle methods for the computation of three-dimensional incompressible unsteady flows, *J. Comput. Phys.* **109**, 247 (1993).
24. C. Zheng and P. P. Wang, *A Modular Three-Dimensional Multispecies Transport Model* (University of Alabama, 1999), http://hydro.geo.ua.edu/mt3d.